ASTRONOMY & ASTROPHYSICS
SUPPLEMENT SERIES

Astron. Astrophys. Suppl. Ser. **118,** 169-179 (1996)

Performance analysis for T.H.E.M.I.S* image stabilizer optical system. I.

(*)Télescope Héliographique pour l'Etude du Magnétisme et des Instabilités de l'atmosphère Solaire

G. Molodij[1,2], J. Rayrole[1], P.Y. Madec[2] and F. Colson[1]

[1] Observatoire de Paris URA 326, C.N.R.S, France
[2] Office National d'études et de Recherche Aerospatiales, BP. 72, 92322 Châtillon Cedex, France

Received April 10; accepted December 19, 1995

Abstract. — This paper describes the performance of the optical image stabilizer system developed for the franco-Italian T.H.E.M.I.S. telescope, which is currently being built on the Canary Island Tenerife. T.H.E.M.I.S will be one of the largest solar telescopes, and will be the first to be manufactured with a real time tip-tilt correction system integrated into its optical train. A new method is described here for measuring image motions. This method is called granulation tracking. It is based on Fourier transform analysis. A servo-loop model is also proposed, based on experimental measurements and the known time properties of atmospheric turbulence, to deduce the image quality obtained after correction. Method sensitivity and accuracy under various terrestrial turbulence conditions are discussed.

Key words: telescopes instrumentation: miscellaneous — atmospheric effects — adaptive — sun: granulation

1. Introduction

The franco-Italian T.H.E.M.I.S. telescope (THEMIS is a French acronym standing for "solar heliographic telescope for the study of solar magnetism and atmospheric instabilities") is designed to obtain very precise measurements of the solar magnetic field vector from simultaneous observations of the sun in a number of different polarized spectral lines. High image quality is an important requirement for the observation of small solar magnetic features like magnetic flux tubes. Spectroscopic diagnostics of the magnetic field, in fact, requires not only a polarization-free telescope and high image quality but al so good image stabilization, so that the light passing through the entrance of the spectrograph slit will come from the same solar structure throughout the observation time.

The harmful motions in the image come from instrument vibrations and steering errors, as well as from random wavefront variations caused by terrestrial atmospheric turbulence. So one of the main optical elements integrated into T.H.E.M.I.S. optical train is a tiltable mirror. Image motion compensation systems are the simplest devices for actively correcting for atmospheric disturbances. These are commonly termed "adaptive optics". The favorable turbulence conditions at the Izana site in the Canary Islands suggests that the 0.9 meter aperture is the best compromise for improving image resolution and stabilizing image displacement, with the use of a tip-tilt mirror (Barletti et al. 1973).

Solar physics research requires observations of magnetic features in a range from one tenth of an arc-second, for flux tubes, to a few arc-minutes, for active regions. Another demand on the image motion compensation system is that the observer should be able to analyze a broad field of view during a time shorter than the solar granulation lifetime (i.e. on a time scale of a few minutes). So, the tip-tilt mirror has a mechanical structure which allows both real time correction of image motions and accurate scanning of the solar surface.

Correlation systems that measure image motions on the sun have been studied for some time now, and several have been developed. The first such system to compensate image motions of a ground-based solar telescope successfully was the breadboard correlation tracker built by the solar physics group at Lockhead's Palo Alto Research Laboratory (Edwards et al. 1987). The NSO/KISS correlation tracker has been in use for several years now (Von Der Luhe et al. 1989) and the I.A.C correlation tracker is installed at the V.T.T German solar telescope (Ballesteros

Send offprint requests to: G. Molodij

et al. 1993).

These trackers operate according to the following principle. Using correlation techniques, successive images are compared with a previously stored reference image to determine their relative displacements in real time. These shifts constitute error signals, which are applied to a tilting mirror in order to correct image motions. The reference image must be updated frequently to account for the morphological variation of the structure being tracked (typically every 60 s with the NSO/KISS correlation tracker) (Von Der Luhe et al. 1989).

In this paper we describe a successfully tested tracking system called a granulation tracker, which stabilizes atmospheric and instrumental image motions. The system allows real time correction while the solar surface is being scanned. The principle is to monitor the variation of the image Fourier transform with respect to some reference, in order to estimate its motions. The two-dimensional Fourier analysis sensitivity is detected by two detectors covering a square field, but with resolution in one direction only, so image motions in the x and y can be estimated independently by monodimentional Fourier transforms. Our studies show that the crosstalk between the two directions is negligible (i.e., the detected displacement in one direction does not depend on the displacement in the other).

The prototype tiltable mirror (29 cm diameter) was developed at the Paris observatory (S.E.R.T and D.A.S.O.P) and has been integrated into the telescope optical train. Servo-loop analysis of the image stabilizer optical system has shown that the effective correction bandwidth is severely limited by the dynamic response of the mirror (with its mechanical eigenfrequencies at 124 Hz and 225 Hz). Moreover, the main characteristic of the system transfer function is the time delay (to read the detectors) inherent in the image motion measurement sampling. This limits the accuracy of the image stabilization due to the very short phase shift in the time delay function (the phase shift is proportional to the frequency). The recent advent of high-speed digital hardware, though, makes it possible to capture solar images at a fast rate (> 500 Hz), which improves stabilization accuracy. Image motions are measured precisely at this rate, as can be seen in recent studies on time characterizations of the atmospheric wavefront. Conan (Conan et al. 1995) gives a cut-off frequency value of 6 Hz for image motion time spectra with a meter-class telescope. These values have been confirmed by experimental data (mean wind velocity of 18 ms^{-1}) (Madec et al. 1992).

In operation, successive image Fourier transforms are estimated at a fundamental frequency and compared at high rate with a reference transform. Our studies show that the system locks on granulation under any seeing conditions. The relative shifts are computed by comparing the Fourier fundamental frequency variation rather than the image of the solar structure directly. This method has been checked in the laboratory, and the system performance has been analyzed. The various system components have been modeled by a time transfer function, which acts as a filter of the incoming turbulent wavefront power spectrum. The dynamic response of the components has been measured experimentally and simulated in order to determine the global time transfer function. Dynamic system control theory (Gille et al. 1967; Demerle 1993; Demerle et al. 1993) is helpful in simulating this transfer function.

The time behavior of the turbulence has been studied by several authors (Clifford 1971; Greenwood & Fried 1976; Greenwood 1977; Roddier et al. 1982; Conan et al. 1992). The main results concerning the angle-of-arrival power spectra are recalled in this paper for use in determining the image stabilizer system performance.

Section 2 presents the overall optical layout of T.H.E.M.I.S. project. The location of the tip-tilt mirror and the granulation tracker along the optical path are discussed. The principle of the granulation tracker is described in Sect. 3. In Sect. 4, the image stabilizer optical system is analyzed: its components are modeled by time transfer functions after experimental measurements. Lastly, in Sect. 5, the theoretical knowledge of the angle-of-arrival time spectra is used to determine the efficiency of the image motion correction.

2. Telescope optical diagram

T.H.E.M.I.S. is a Richtey-Chretien telescope supported by an azimuthal mount (Fig. 1). It is evacuated, and closed by two windows. When the main beam enters the polarization analyzer at the primary focus F1, (equivalent focal length of 17 meters, F/17), the pupil image is at infinity. The polarization analyser, located at focus F1, comprises three parts: two achromatic quarter-wave plates and a polarizing beam splitter. The beam splitter axes are oriented at 45 degrees with respect to the spectrograph entrance slit. The axes of the two quarter-wave plates are oriented so that the three Stokes parameter combinations $I+V$ and $I-V$, $I+U$ and $I-U$, $I+Q$ and $I-Q$ are obtained at the analyzer output (Fig. 1). The subsequent optics are designed to transfer the two useful beams coming out of the analyzer along close optical paths. These transfer optics include a concave mirror, M3 (which might be used for autofocus mode correction in the future adaptive optics system), a 45 degree flat mirror, M4, and the tip-tilt mirror M5 (Fig. 2) placed in a pupil plane image focussed by the mirror M3.

Then comes an imaging device (M6, M7) combined with a field rotator and field corrector to produce an enlarged image on the spectrograph entrance slit (focus F2, equivalent focal length of 57 meters, F/63).

In F2, the polarization analyser produces two images of the window in front of the polarization analyser (focus F1). The length of the image is 2 arc-minutes, and the width can be adjusted from 2 to 12 arcsecond depending

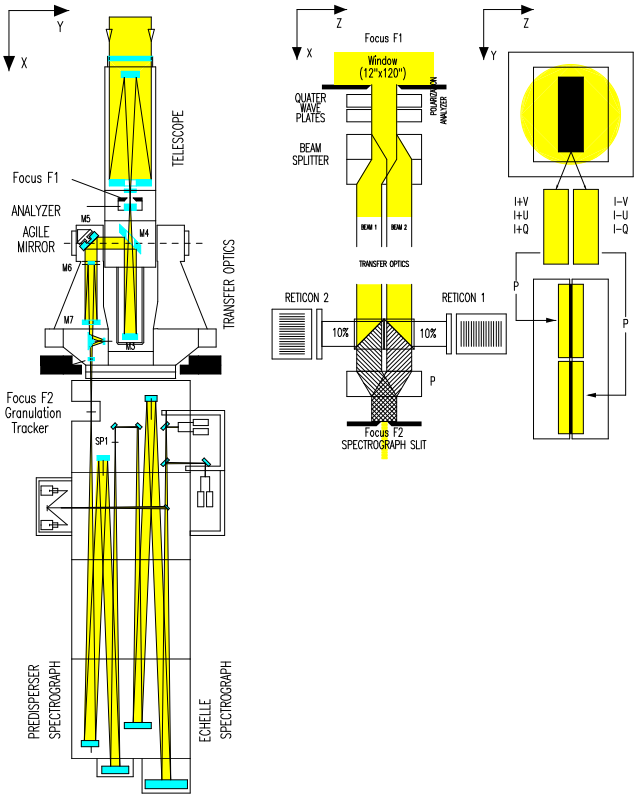

Fig. 1. T.H.E.M.I.S optical scheme: On the left is the main optical path inside the mechanical structure of the instrument, showing the location of the polarization analyser, the tip-tilt mirror, and the granulation tracker. In the middle is the polarization analyzer (focus F1) with the two quarter-wave plates and the polarizing beam splitter. Just in front of the spectrograph entrance slit (focus F2) 10% of the light is used for the two Reticon diode array detectors of the granulation tracker. On the right, the two useful beams (90%) are adjusted along the spectrograph entrance slit by means of the optical prism device P

on the Fried parameter r_0. In front of the spectrograph entrance slit, 10% of the light is used for the two "reticon" diode arrays of the granulation tracker. The two useful beams (90% of the light) are adjusted along the spectrograph slit by means of an optical prism device so that the two spectra, for the two beams transmitted by the polarization analyser, will be completely separated at the spectrograph focus (SP2) .

The spectrograph hangs vertically from the same part as the azimuthal mount of the telescope. Both beams enter the long predisperser and pass through the collimator, which can compensate astigmatism aberrations. Three different gratings can be exchanged automatically in the predisperser (one of them is an echelle grating) (Mein & Rayrole 1991).

In the basic configuration, masks can be put in the plane of the intermediate focus (SP1) in order to select a number of spectral lines. The large camera mirror of the echelle spectrograph produces high dispersion spectra simultaneously for the entire spectral range selected in the predisperser focus (SP1) of the two beams transmitted by the polarization analyser.

The last transfer optics (to adjust the size of the pixel) and the detectors are placed at the focus (SP2) of this spectrograph. The basic configuration includes twenty C.C.D cameras (288×384 pixels), which are necessary to record ten line profiles simultaneously in two Stokes parameters along 384 solar points. The tip-tilt mirror and image stabilizer optical system are integrated into the T.H.E.M.I.S optical train at manufacture, to correct the wavefront perturbations caused by terrestrial atmospheric turbulence. The mirror structure is summarized as follows (Fig. 2):

1) self-adjusting optical support, to integrate the mirror in the optical set-up.
2) light, rigid 29 cm diameter mirror.
3) optical-mechanical connection.
4) mirror supports: three arms separated by 120 degrees to scan a solar field of 4×4 arcminutes moving the tip-tilt mirror with elastic axis.
5) two piezo-electric quartz actuator supports: two arms at 90 degrees.
6) two elastic axis for tilting and scanning functions.

The optical system is mainly conceived as a solar image stabilizer, and has a scanning utility in order to allow an accurate measurement of the spatial derivative of solar physics parameters during the observations.

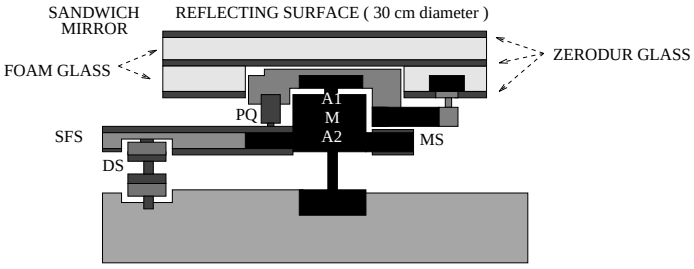

Fig. 2. Tip-tilt mirror structure. M: master piece with two elastic axes (A1, A2); A1: axis for tilting function (±3 arcsec); A2: axis for scanning function (±2 arcmin); PQ: two piezo-electric quartz actuators at 90 degrees; MS: mirror support, three arms at 120 degrees; SFS: support for scanning function, two arms at 90;degrees, DS: double screw for scanning function. The mechanical structure makes it possible to scan a solar field of 4×4 arcminutes moving the tip-tilt mirror slowly with the axis scanning function

3. Granulation tracker

3.1. *Principle*

In this section, we present a new method for measuring image motions by which extensive sources can control the tip-tilt mirror in real-time.

The tracking method, like the correlation tracking method, is based on comparing a reference picture of the area of interest on the sun with the instantaneous pictures scanned by the detector. The shifts measured constitute error signals, which are applied to a tilting mirror that corrects the relative displacements in real-time.

The image is detected by two detectors (Reticon 128 s photo-diode arrays), which cover a square field together but which each have resolution in one direction only. The reticon has elongated 2500 × 25-micron pixels that are sensitive to motion in the direction of the smaller diode dimension. The images seen by the diode arrays are the convoluted samples of the granulation images through a window the size of the pixels. Since the pixels are elongated, the loss of resolution will be different depending on the direction (Fig. 3). Our laboratory tests show that the crosstalk between the two directions is negligible using this method (i.e, the detected displacement in one direction does not depend on the displacement in the other). So, the image motions detected by each photo-diode array in two perpendicular directions are independent and can be analyzed separately.

The granulation tracker, incorporated in the T.H.E.M.I.S. optical arrangement, has been designed to work with the polarization analyser (Rayrole 1992). In this polarimetric mode two beamsplitters in front of the spectrograph entrance slit send 10% of the light from each of the two beams coming from the polarization analyser to the linear photo-diode arrays (Figs. 1 and 4). In the granulation image, the cross-section of the two arrays defines a square field-of-view of size "L" which can be adjusted from 2×2 arcseconds to 12×12 arcseconds, depending on the Fried parameter r_0.

Let us point out that the calculation of two one-dimensional Fourier transforms at a given frequency requires far fewer operations than the calculation of a two-dimensional covariance.

The two instantaneous pictures are generated by two linear detectors and characterized by their one-dimensional intensity distribution $I(r + d_r)$ where d_r denotes an arbitrary spatial lag. We wish to detect its shift compared to the same unshifted reference image $I(r)$ by means of a discrete Fourier transform. Both r and d_r are measured in some units related to the spatial scale, i.e., arcsec on the solar surface. We take N equidistant spatial samples with steps Δr over the field $R = N\Delta r$.

The discrete Fourier transform at the j^{th} order of an image

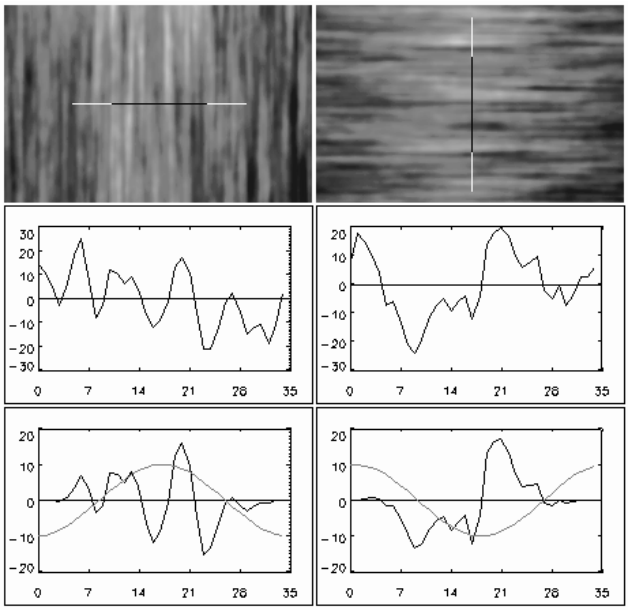

Fig. 3. Top: the granulation image seen by the two diode arrays. The white line shows the length of the arrays and the black one the common array field of view adjusted to 7 arcsecond. Middle, the signals delivered by the two diode array detectors (on the left reticon x, on the right reticon y). Bottom, the signals are multiplied by a Hanning function and the sine function adjusted in order that the imaginary part of the Fourier transform coefficient is null

granulation $I(r)$ is then given by:

$$a_j = \frac{1}{N}\sum_{k=0}^{N-1} I(k\Delta r)\mathrm{e}^{-2i\pi jk\frac{\Delta r}{R}} = \frac{1}{N}\sum_{k=0}^{N-1} I(k\Delta r)\mathrm{e}^{-2i\pi j\frac{k}{N}} \tag{1}$$

Invoking the shift theorem of Fourier transforms (Roddier 1971), we have:

$$\begin{aligned}\frac{1}{N}\sum_{k=0}^{N-1} I(k\Delta r + d_r)\mathrm{e}^{\left(-2i\pi jk\frac{\Delta r}{N}\right)} &= \frac{1}{N}\sum_{k=0}^{N-1} I(k\Delta r)\mathrm{e}^{\left(-2i\pi j\frac{(k\Delta r + d_r)}{R}\right)} \\ &= \frac{1}{N}\sum_{k=0}^{N-1} I(k\Delta r)\mathrm{e}^{\left(-2i\pi j\left(\frac{k}{N}+\frac{d_r}{R}\right)\right)}\end{aligned} \tag{2}$$

At the fundamental frequency $j = 1$, the discrete Fourier transform of the shifted image is given by invoking Euler's formula:

$$\begin{aligned}a_1 &= \frac{1}{N}\sum_{k=0}^{N-1} I(k\Delta r)\mathrm{e}^{\left(-2i\pi\left(\frac{k}{N}+\frac{d_r}{R}\right)\right)} \\ &= \frac{1}{N}\sum_{k=0}^{N-1} I(k\Delta r)\left[\cos\left(2\pi\left(\frac{k}{N}+\frac{d_r}{R}\right)\right) - i\sin\left(2\pi\left(\frac{k}{N}+\frac{d_r}{R}\right)\right)\right]\end{aligned} \tag{3}$$

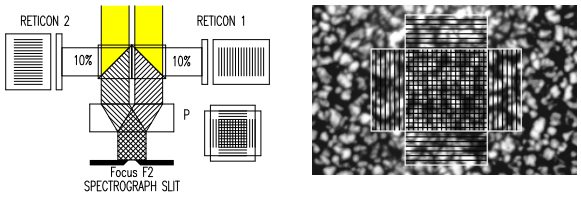

Fig. 4. Granulation tracker optical scheme. In polarimetry mode, the two beams coming from the polarization analyser are used by the tracker. Each beam splitter sends 10% of the light to the Reticon array, which has elongated pixels of size 2500 × 25 microns (left). Averaging the intensity fluctuations in the large photo-diode size direction, the image motions are detected in the perpendicular direction. On the right, the cross-section of the two Reticon arrays defines a grid with a field of view which can be adjusted from 2 × 2 up to 12 × 12 arcseconds, depending on the Fried parameter value

Let us consider only the imaginary part of Eq. (3) at the fundamental frequency denoted σ. During the initialization phase, we select the origin of the spatial coordinate system such that the imaginary part of the fundamental Fourier component vanishes for the unshifted image; i.e.,

$$\sigma = \frac{1}{N} \sum_{k=0}^{N-1} I(k\Delta r)\ \sin\left(2\pi \frac{k}{N}\right) = 0 \tag{4}$$

and, therefore,

$$a_1 = \frac{1}{N} \sum_{k=0}^{N-1} I(k\Delta r)\ \cos\left(2\pi \frac{k}{N}\right) \tag{5}$$

During the operative phase, the instantaneous image of the granulation is d_r shifted. So, σ is given by:

$$\begin{aligned} \sigma &= \frac{1}{N} \sum_{k=0}^{N-1} I(k\Delta r)\ \sin\left(2\pi\left(\frac{k}{N} + \frac{d_r}{R}\right)\right) \\ &= \sin\left(2\pi \frac{d_r}{R}\right)\ \frac{1}{N} \sum_{k=0}^{N-1} I(k\Delta r)\ \cos\left(2\pi \frac{k}{N}\right) \\ &= \sin\left(2\pi \frac{d_r}{R}\right)\ a_1 \end{aligned} \tag{6}$$

As expected, the intensity distribution of observed structures varies in successive images, due to atmospheric disturbances of the wavefront. Certain granules move into or out of the field of view. So, a differential measurement must be applied to extract the correct signal error.
Two values of σ are computed with a shift of $\pm\ 2\Delta r$:

$$\begin{cases} \sigma_{+2} = \sin(\frac{2\pi(d_r+2)}{N})\ a_1 \\ \sigma_{-2} = \sin(\frac{2\pi(d_r-2)}{N})\ a_1 \end{cases} \tag{7}$$

Then, a normalized quantity D_r of slight independent fluctuations is extracted:

$$D_r = \frac{\sigma_{i+2} - \sigma_{i-2}}{\sigma_{i+2} + \sigma_{i+2}} = \frac{\sin(\frac{2\pi(d_r+2)}{N}) - \sin(\frac{2\pi(d_r-2)}{N})}{\sin(\frac{2\pi(d_r+2)}{N}) + \sin(\frac{2\pi(d_r-2)}{N})} \tag{8}$$

At a fast operative rate, the shifts are small quantities. Considering the limited development at the first order of the sine function, we have:

$$D_r = \frac{d_r}{2} \tag{9}$$

The relative displacement in the direction r can be calculated from the relative shift of the sine function with respect to the reference.
Nevertheless, the method raises certain problems in practice, due to the fact that the Fourier analysis is performed on a non-periodic intensity function. The granulation Fourier image has frequencies below the fundamental determined from the size L of the field-of-view. So a Hanning function is applied in order to have a periodic signal. The method used to extract the correct signal error has been tested in the laboratory (Rayrole 1992). The values of σ_{xi} and σ_{yi} are given by:

$$\begin{cases} \sigma_{xi} = \sum_{\text{pixels } x} (I(x) - M_x)\ H(x)\ \sin(x + r_x) \\ \sigma_{yi} = \sum_{\text{pixels } y} (I(y) - M_y)\ H(y)\ \sin(y + r_y) \end{cases} \tag{10}$$

$*$) $I(x)$ and $I(y)$ are the signals sampled by the diode arrays inside the common part of the analyzed field of view, of size LxL.
$*$) M_x and M_y are the corresponding intensity mean values.
$*$) $H(x)$ and $H(y)$ are Hanning apodization functions, used to suppress Fourier frequencies below the fundamental frequency calculated from the size L of the window (i.e, the signal is periodic on L) (Fig. 3) .
This novel method for determining image motions at a high rate (image sampled at 582 Hz) has the advantage of being possible on common processors like the T.M.S 32020.
Let us point out that, in high resolution spectroscopic observations, it is not enough to have a stabilized image of the sun on the spectrograph entrance slit, we must also be able to adjust the smallest details of the stabilized image inside the slit. This is easy to do when the sine function is computed with a more accurate sample step (0.02 arcseconds on the sky for instance). The values of r_x and r_y can be adjusted in a closed-loop and, by increasing or decreasing r_x or r_y by one unit, the stabilized image can be move in steps of 0.02 arcseconds.

3.2. *Signal detection and noise considerations*

The granulation images seen by the photo-diode arrays (Fig. 3) show a low-contrast intensity structure in the direction of the smallest pixel dimension, and large elongated structures along the perpendicular direction. Image

motion detection is limited by the contrast of the structures seen by the reticon, and possibly disturbed by the global noise.

Actually, the signal contrast will depend not only on the pixel size but also on the atmospheric turbulence. Methods using the rms contrast of solar granulation to determine the Fried parameter r_0 are discussed by Ricort et al. (Ricort et al. 1981; Ricort et al. 1982).

We adopt the theoretical model based on results obtained from solar speckle interferometry to analyze the performances of the granulation tracker under various turbulence conditions. As presented by Ricort et al., the relationship between the variance of the observed brightness fluctuations $(\Delta I)^2_{\rm rms}$ and the Fourier transform of the intensity distribution $\hat{O}^2(\boldsymbol{f})$ is expressed by the relation:

$$(\Delta I)^2_{\rm rms} = \int \hat{O}^2(\boldsymbol{f})\ {\rm FTS}(\boldsymbol{f})\ {\rm d}\boldsymbol{f} \qquad (11)$$

where ${\rm FTS}(\boldsymbol{f}) =< ({\rm FTO})^2_{\rm se} >$ is the speckle transfer function defined as the average of short-exposure transfer functions.

The granulation tracker reduces the brightness fluctuations in the image focus, and Eq. (11) becomes:

$$(\Delta J)^2_{\rm rms} = \int \hat{O}^2(\boldsymbol{f})\ {\rm FTS}(\boldsymbol{f})\ P^2(\boldsymbol{f})\ {\rm d}\boldsymbol{f} \qquad (12)$$

where $P^2(\boldsymbol{f})$ corresponds to the Fourier transform square modulus of a window of pixel size.

The speckle interferometric techniques applied to solar granulation by Ricort and Aime yield a radial expression for $\hat{O}^2(\boldsymbol{f})$ denoted $W_0(f)$, written in analytic form as:

$$W_0(f) = 0.019\ (1 - 0.68\ {\rm e}^{-10f^2})\ {\rm e}^{-1{,}88f} \qquad (13)$$

By simulating the phase developed on the set of Zernike polynomials, as first proposed by N. Roddier (1991), the speckle transfer function can be estimated for computing $(\Delta I)^2_{\rm rms}$ and $(\Delta J)^2_{\rm rms}$.

This simulation has been developed at O.N.E.R.A (Rousset et al. 1991; Conan 1995) in accordance with theoretical expressions given by Korff (1973).

Figure 5 shows the optimum contrast $(\Delta I)^2_{\rm rms}$ for a 90 cm telescope aperture for various values of Fried parameter r_0, and the detection limit corresponding to the global noise ($S/N = 300$). The granulation tracker reduces the contrast by a factor of three under favorable turbulence conditions ($r_0 = 25$ cm). Under unfavorable conditions, the relative contrast loss is always less a factor of about two. So regardless of the amount of atmospheric turbulence, the granulation tracker always helps image motion detection to a certain extent.

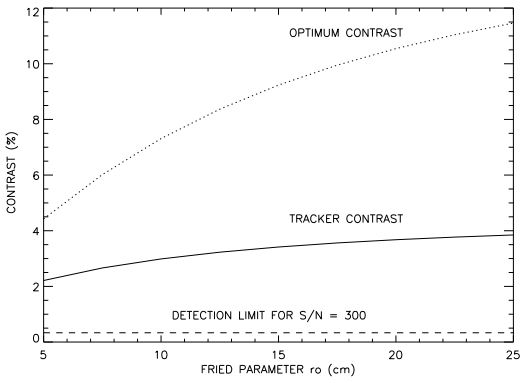

Fig. 5. Variation of the contrast fluctuations versus the Fried parameter r_0. The solid curve corresponds to optimum contrast and the dashed one shows the contrast measured by the pixel diode arrays dimensioned at $6 \times 0,1$ arcsecond. The signal-to-noise ratio is $S/N = 300$. The noise is not a limitation for the granulation tracker analysis

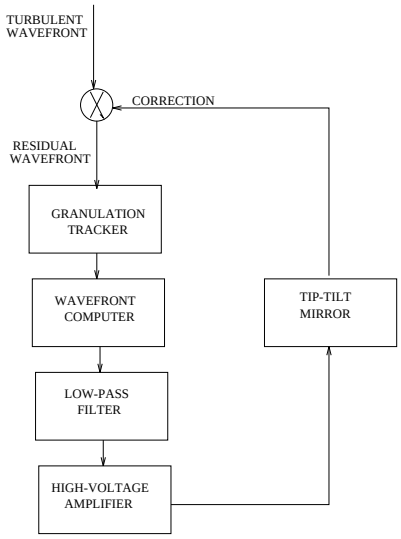

Fig. 6. Fast image motion compensation system block diagram

4. Overall transfer function modeling

In this section, the formalism described provides a simple modeling of the time behavior of the image stabilizer optical system. Our system consists of (Fig. 6):

- granulation tracker
- wavefront computer
- low-pass filter
- high voltage amplifier
- tip-tilt mirror.

The granulation tracker, which measures the image

displacements, is characterized by its integration time, denoted T. It defines the sampling rate of the image motion measurements, and then the sampling frequency of the closed-loop system. A real-time computer based on T.M.S 32020 processor is used to compute the image motions and calculate the tip-tilt mirror control voltages. The high voltage amplifiers bring a power supply to move the piezoelectric actuators from the measurements calculated by the computer.

In the linear system hypothesis, we use the Laplace transform for the continuous representation with the Laplace variable S (Gille et al. 1967).

The granulation tracker sensor transfer function can then be modeled by:

$$\mathrm{GT}(S) = \frac{1 - \mathrm{e}^{-T.S}}{T.S} \tag{14}$$

The real-time computer applies algorithms to deduce image displacements to activate the tip-tilt mirror. These calculations are characterized by a time delay T_{calc}. Nevertheless, we have also to take into account the time delay needed to read down all the photo-diodes before beginning the calculations $T_{\mathrm{photo-diodes}}$.

Lastly, the transfer function corresponding to the time delay $T_{\mathrm{delay}} = T_{\mathrm{calc}} + T_{\mathrm{photo-diodes}}$ is expressed as:

$$\mathrm{WC}(S) = G_{\mathrm{computer}}\ \mathrm{e}^{-T_{\mathrm{delay}}.S} \tag{15}$$

where G_{computer} is the gain determined by the computer during signal processing. The high voltage amplifier analogic integrator continuously drives the mirror's piezoelectric actuators. Its transfer function is: $1/S$.

The dynamic response of the tip-tilt mirror has been characterized by measuring its transfer function from the controlled random noise of a spectrum analyser. The behavior of this device is given by its mechanical response, characterized by eigenfrequencies. Assuming the linearity properties, the transfer function of the tip-tilt mirror is given by the product of second order filters.

Experimental measurements show two strong resonant peaks at $f_1 = 124$ Hz and $f_3 = 225$ Hz and anti-resonant peak at $f_2 = 140$ Hz. Then, the mirror transfer function, denoted $M(S)$ is given by:

$$M(S) = M_1(S)\ M_2(S)\ M_3(S) \tag{16}$$

$$\text{with} \begin{cases} M_1(S) = \frac{\omega_1^2}{\omega_1^2 + 2\zeta_1\omega_1.S + S^2}, \omega_1 = \frac{1}{2\pi f_1}, \zeta_1 = 0.03 \\ M_2(s) = \frac{\omega_2^2 + 2\zeta_2\omega_2.S + S^2}{\omega_2^2}, \omega_2 = \frac{1}{2\pi f_2}, \zeta_2 = 0.05 \\ M_3(s) = \frac{\omega_3^2}{\omega_3^2 + 2\zeta_3\omega_3.S + S^2}, \omega_3 = \frac{1}{2\pi f_3}, \zeta_3 = 0.15 \end{cases}$$

The presence of strong resonances at the mechanical structure's eigenfrequencies induces closed-loop instabilities and requires the use of a low pass filter. This first order filter reduces the bandwidth by introducing a cutoff frequency denoted f_{c}. Its transfer function is given by:

$$\mathrm{LPS}(S) = \frac{1}{1 + a.S} \text{ where } a = \frac{1}{\omega_{\mathrm{c}}} = \frac{1}{2\pi f_{\mathrm{c}}} \tag{17}$$

The servo loop block diagram is shown in Fig. 7, where ϕ_{turb} are image displacements due to atmospheric disturbances and ϕ_{res} the residual error, which is the difference between ϕ_{turb} and corrective signal and the correcting term applied by the tip-tilt mirror, ϕ_{cor}.

As a result of the previous modeling, the overall system

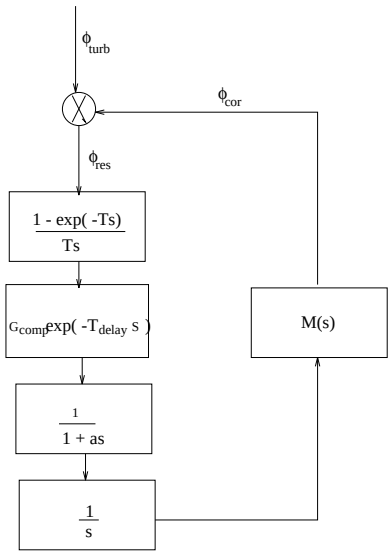

Fig. 7. Servo loop block diagram

can be represented by its transfer function, denoted $G(S)$.

$$G(S) = G_{\mathrm{computer}} \left[\frac{1 - \mathrm{e}^{-T.S}}{T.S^2} \frac{\mathrm{e}^{-T_{\mathrm{delay}}}}{1 + a.S} \cdot \frac{\omega_1^2\omega_3^2(\omega_2^2 + 2\zeta_2\omega_2.SS^2)}{\omega_2^2(\omega_1^2 + 2\zeta_1\omega_1.S + S^2)(\omega_3^2 + 2\zeta_3\omega_3.S + S^2)} \right] \tag{18}$$

with $T = 1.72$ ms (sampling frequency of 582 Hz). $T_{\mathrm{delay}} = 3.12$ ms, a $= \frac{1}{2\pi f_{\mathrm{c}}}$ with first order filter cut-off frequency $f_{\mathrm{c}} = 300$ Hz.

The open-loop dynamic response of the image stabilization system was measured experimentally, using a spectrum analyser, and compared with the theoretical transfer function $G(S)$ (Fig. 8). The model is in very good agreement with the measurements, and shows a strong resonant peak at 124 Hz. Nevertheless, one compensated closed loop performance requirement is to have a band as wide as possible to improve disturbance rejection, within the limits of loop stability. These constraints mean the "G_{computer}" and low-pass filter cut-off frequency must be chosen.

The optimum gain and filter cutoff frequency can be determined from dynamic systems control theory such that $G(S)$, plotted in the Black abacus, is as close as possible to the 2.3 dB curve. This ensures a good trade-off between stability and accuracy. Figure 9 presents the optimum transfer function $G(S)$ with a low-pass filter cutoff

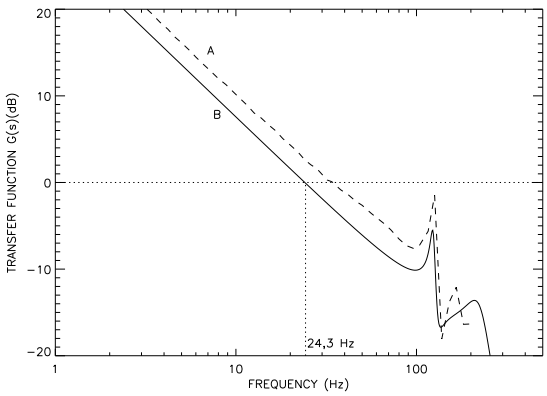

Fig. 8. Comparison between the theoretical transfer function $G(s)$ (curve B) and the open-loop dynamic response measured experimentally (curve A) (to distinguish the data, curve A is shifted). It shows a strong resonant peak at 124 Hz and a useful bandwidth of 24.3 Hz at 0 dB

frequency at 300 Hz. A useful bandwidth of 24.3 Hz is shown at 0 dB.

Conventionally, the control loop servo bandwidth is defined as the closed-loop cutoff frequency at -3 dB. This transfer function is defined as the ratio between the output signal $\phi_{\rm cor}$ and the input signal $\phi_{\rm turb}$. This ratio, represented in Fig. 10, is given by:

$$\frac{\phi_{\rm cor}(S)}{\phi_{\rm turb}(S)} = \frac{G(S)}{1+G(S)} \tag{19}$$

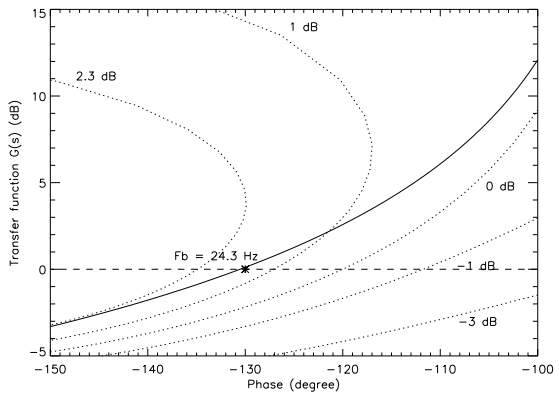

Fig. 9. The Black abacus can be used to determine the optimum gain $G_{\rm comp}$ and the minimum low-pass filter cutoff frequency for stable closed-loop in order to obtain a maximum bandwidth. The transfer function $G(s)$ is as close as possible to the 2.3 dB curve showing a useful bandwidth of 24.3 Hz. The different dashed curves correspond to Black curves extracted from dynamical system control theory

The Bode diagram in Fig. 10 shows a cutoff frequency of 60 Hz at -3 dB.

The rejection transfer function is equal to the ratio between the residual error $\phi_{\rm res}$ and the input signal $\phi_{\rm turb}$. It defines the system correction efficiency as a function of the frequency. It is given by the expression:

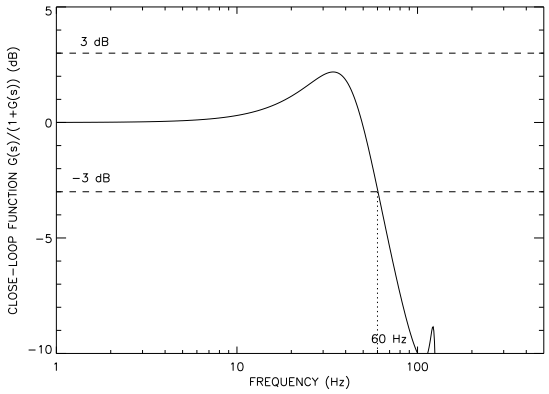

Fig. 10. The Bode diagram of the closed-loop $G(s)/(1+G(s))$ shows a bandwidth of 60 Hz at -3 dB

$$\frac{\phi_{\rm res}(s)}{\phi_{\rm turb}(S)} = \frac{1}{1+G(S)} \tag{20}$$

The corresponding Bode diagram (Fig. 11) shows a useful bandwidth of 21 Hz at 0 dB. For any sinusoidal input of frequency lower than 21 Hz, the residual error magnitude is less than the input magnitude.

Let us note that the useful bandwidth of 21 Hz, and the closed-loop stability, are dominated by the strong resonances corresponding to the mechanical structure's eigenfrequencies. Our studies show that insignificant gain in bandwidth is obtained by reducing the signal sampling rate or reducing the time delay calculation. Nevertheless, performance analysis shows the efficiency of the system in compensating fast image motions in real-time.

5. Performance analysis

In order to determine the efficiency of the image motion correction by our image stabilizer optical system, we will review here some data concerning the time characterization of atmospheric turbulence. Several authors have studied the time behavior of turbulence from a theoretical point of view (Clifford 1971; Greenwood & Fried 1976; Greenwood 1977), and a number of publications have presented experimentally measured power spectra of image motion or angle of arrival (Martin 1987; Soules et al. 1989). Conan (1995) has calculated the theoretical angle of arrival power spectra and found that they exhibit a sharp cutoff around the frequency $\nu_{\rm c}$ of the order of 0.3

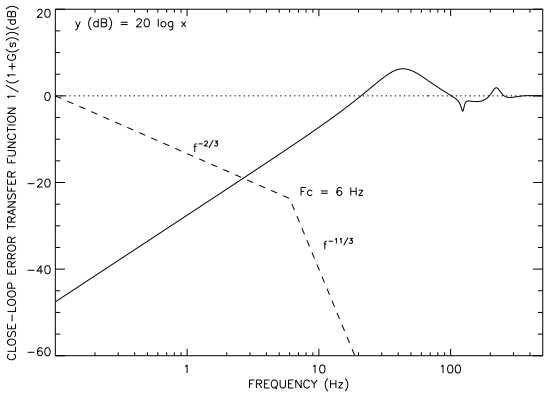

Fig. 11. The rejection transfer function is represented in solid line and shows an effective bandwidth of 21 Hz at 0 dB. The theoretical angle of arrival power spectrum is plotted (in dB) in a dashed curve. Below the cut-off frequency F_c, the spectrum is represented by a $-2/3$ power law and by a $-11/3$ power law above F_c (from J.M. Conan (1995)). For an 18 ms^{-1} turbulence wind velocity (average condition) and 0.9 m telescope aperture, $F_c = 6$ Hz

V/D where V is the mean wind velocity along the propagation path and D the telescope aperture. The frequencies beyond the cutoff are attenuated as a consequence of the pupil filtering. The spectrum follows a power law of $\nu^{-11/3}$ at high frequencies and a $\nu^{-2/3}$ law below the cutoff. The theoretical angle of arrival $\phi_{\rm turb}(f)$ spectrum is plotted (in dB) in Fig. 11.

The theoretical characterization of angle of arrival is an issue for the evaluation of the efficiency of the image stabilisation. The effect of the image stabilizer optical system is well described by a time filtering of the image motion spectrum by the rejection transfer function square modulus. The residual variance σ^2_ϕ of the image displacement is given by the integral over the frequency range of its power spectrum after correction, which is the product of the turbulent power spectrum by the rejection tranfer function square modulus:

$$\sigma^2_{\phi_{\rm res}} = \int_0^\infty |\phi_{\rm res}(f)|^2 \, {\rm d}f = \int_0^\infty \frac{|\phi_{\rm turb}(f)|^2}{|1+G(f)|^2} \, {\rm d}f \quad (21)$$

Let us remember that angle-of-arrival fluctuations, introducing the Fried parameter ro, for a telescope aperture D, are expressed by (Roddier 1981):

$$\sigma^2_\alpha \ ({\rm rad}^2) = 0.174 \, \lambda^2 \, r_0^{-5/3} \, D^{-1/3} \quad (22)$$

We computed the standard deviation numerically from Eqs. (6-8) with and without correction σ_α versus the Fried parameter r_0 that characterizes the atmospheric turbulence conditions (Fig. 12). Our analysis shows the efficiency of the image stabilization. The granulation tracker is able to control the tip-tilt mirror under different atmospheric conditions. Figure 12 also shows the efficiency of the system to compensate fast image motions in real-time for a meter-class telescope in the average case of turbulence.

Nevertheless, the standard deviation after motion correction is not a properly measure of image quality at the spectrograph slit entrance, but only of the optical system capability to immobilize granulation images. Actually, for small values of r_0 parameters, the optics system corrects image motions but does not improve its sharpness (corrugation due to higher orders like defocus, astgmatism, ...). Fried (1966) calculates the integral of the mean modulated transfer function denoted R (proportional to the Strehl ratio (O'Neill 1963) to determine the image quality.

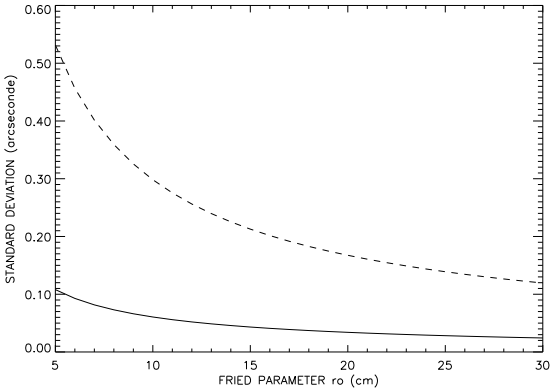

Fig. 12. Standard deviation of image motion (arcsecond) versus the Fried parameter r_0. The solid line shows standard deviation after correction compared with standard deviation without correction (dash curve). They are calculated for a telescope aperture $D = 0.9$ meter, a wavelength $\lambda = 0.5$ μm, and a mean wind turbulence velocity $V = 18$ ms^{-1}

$$R = \int \tau(\boldsymbol{f}) \, {\rm d}\boldsymbol{f} = \int \tau_0(\boldsymbol{f}) \, B(\boldsymbol{f}) {\rm d}\boldsymbol{f} \quad (23)$$

introducing the phase structure function $D_\phi(\lambda, \boldsymbol{f})$ with:

$$B(\boldsymbol{f}) = \exp\left[-\frac{1}{2} \, D_\phi(\lambda, \boldsymbol{f})\right] = \exp\left[-3,44 \left(\frac{\lambda \boldsymbol{f}}{r_0}\right)^{\frac{5}{3}}\right] \quad (24)$$

with λ being the light wavelength and $\tau_0(\boldsymbol{f})$ the telescope transfer function without turbulence.

To evaluate the image quality after the image motion correction, the integral of the modulated transfer function can be calculated for the short exposure case. The center of gravity fluctuations are defined by a Gaussian statistical law. So R is given by Fried (1966):

$$R = \int \tau_0(\boldsymbol{f}) \ \exp\left[-3,44 \left(\frac{\lambda \boldsymbol{f}}{r_0}\right)^{\frac{5}{3}} \left(1 - \frac{\lambda \boldsymbol{f}}{D}\right)^{\frac{1}{3}}\right] \quad (25)$$

with D being the telescope aperture.
The telescope angular resolution through atmospheric turbulence is defined by Roddier (1981) as:

$$\omega = \left(\frac{4}{\pi R}\right)^{\frac{1}{2}} \tag{26}$$

and without atmospheric perturbations by:

$$\omega_{\rm d} = \frac{4}{\pi}\frac{\lambda}{D} = 1,27\frac{\lambda}{D} \tag{27}$$

Figure 13 shows the angular resolution expressed in units of $\omega_{\rm d}$ for a stabilized image, compared with the uncorrected case. For $\frac{D}{r_0}$ ratio $\simeq$ 3,5 (r_0 = 26 cm), the image distortion can be considered to be essentially due to tilts of the wavefront, and the motion correction reduces the image sharpness. For small values of r_0, one can not reach telescope diffraction limit with the image stabilization correction alone.
The time characterization of turbulent wavefronts is at issue in the choice of servo-loop bandwidth in the adaptive optics sytem. In our model, the rejection transfer function square modulus behaves as ν^2 at low frequencies (below the error function bandwidth fb = 21 Hz) and saturates at the value of unity above that bandwidth, which means that there is no more compensation at high frequency. This bandwidth is larger than the time angle-of-arrival spectrum cutoff frequency, of the order of 6 Hz (at a meter-class telescope in the average case).

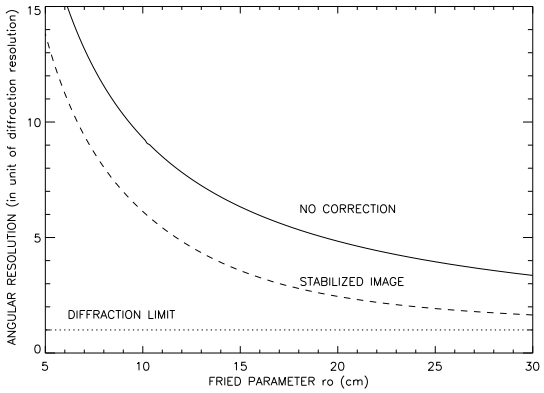

Fig. 13. Resolution $\frac{\omega}{\omega_{\rm d}}$ versus the Fried parameter r_0 (cm). The dash line shows the resolution for image stabilization correction compared with the resolution without correction (solid curve). The angular resolution reaches the diffraction limit (0.145 arcsecond with telescope aperture D = 0.9 meter and a wavelength λ = 0.5 μm). For $\frac{D}{r_0} < 3$, the distortion can be considered to be essentially tilts of the wavefront

6. Conclusion

In this paper, we present a time modeling of the T.H.E.M.I.S. image stabilizer optical system for the adjustement of experimental parameters such as exposure time, sampling frequency, bandwidth, electronic filters, and so forth. The simulation is validated with experimental measurements. We have used the time characterization of turbulent wavefronts to estimate the accuracy of the image stabilization needed in high-resolution spectroscopic solar observations.
We also describe a wavefront sensor based on an original principle of granulation tracking which is well suited for incoherent sources, telescope aperture, and unfavorable turbulence conditions.
Nevertheless, effects of anisoplanatism are not considered in the present paper. It is understood that anisoplanatism poses a severe problem if the field of view of the tracker is not cut down to approximately the isoplanatic patch. More detailed study is necessary to understand all the effects that might arise from such a situation.
Second, the granulation tracker will successfully operate under any seeing conditions. But it must be kept in mind that the granulation tracker system makes wavefront slope measurements in order to correct pure wavefront tilts, so the previous analysis is insufficient to estimate the errors made using the image stabilizer optical system.
We will be presenting an analysis of such problems in another paper, and will present an estimate of image quality after correction using the T.H.E.M.I.S. image stabilizer optical system in imagery and spectroscopy modes. We will determine the isoplanatic domain when observing extended source and adaptibility of the granulation tracker depending on the Fried parameter ro.

Acknowledgements. The authors are grateful to P. Gigan for his help in the experiments, to R. Muller for granulation images of the sun, and to J.M. Conan for his valuable comments.

References

Ballesteros E., Viera T., Lorenzo F., et al., Cargese 29 juin-9 juillet 1993 NATO proceedings
Barletti R., Ceppatelli G., Moroder E., Paterno L., Righini A., 1973, Site testing at Tenerife by ballon borne radiosonder and optical quality of the atlantic air mass over the Canary Island, J.O.S.O annual report
Clifford S.F., 1971, J. Opt. Soc. Am. A. 61, 1285
Conan J.M., Madec P.Y., Rousset G., 1992, "Temporal power spectra of turbulent wavefronts" 13 th Sacramento Peak Summer Workshop on Real Time and Post-Facto Solar Image Correction
Conan J.M., 1995, J. Opt. Soc. Am. 12, 1559-1570
Demerle M., Cargese 29 juin-9 juillet 1993 NATO proceedings
Demerle M., Madec P.Y., Rousset G. Cargese 29 juin-9 juillet 1993 NATO proceedings

Edwards C.G., Levay M., Gilbreth C.W., et al., 1987, Bull. Am. Astron. Soc. 19, 929
Fried D.L., 1966, J. Opt. Soc. Am. 56, 1372-1379
Gille J. Ch., Decaulne P., Pelegrin M., 1967, Theorie et calcul des asservissements lineaires. Edition Dunod
Korff D., 1973, J. Opt. Soc. Am. 63, 971-980
Greenwood D.P., Fried D.L., 1976, J. Opt. Soc. Am. A. 66
Greenwood D.P., 1977, J. Opt. Soc. Am. 67, 390-392
Madec P.Y., Conan J.M, Rousset G., 1992, in Proceedings of E.S.O Conf.42 on Progress in Telescope and Instrumentation technologies. In: Ulrich M.H (ed.) Garching bei Munchen, Germany, p. 471-474
Martin H.M., 1987, PASP 99, 1360-1370
Mein P., Rayrole J., 1991, A&A 248, 669
O'Neill E.L., 1963, in: Addison, Wesley (ed.), Primot J., 1989, Thesis Paris XI
Rayrole J., 1992 (private communication)
Ricort G., Aime C., Roddier C., Borgnino J., 1981, Solar Phys. 69, 222
Ricort G., Borgnino J., Aime C., 1982, Solar Phys. 75, 377
Roddier F., 1971, Ediscience Paris (Ed.)
Roddier F., 1981, in Prog. in Opt. XIX, North-Holland Publishing Co (Amsterdam). In: E Wolf (ed.), p. 281-376
Roddier F., Gilli J.M , Lund G., 1982, J. Opt. (Paris) 13, p. 263-271
Roddier N., 1990, Opt. Eng. 29, p. 1174-1180
Rousset G., Primot J., Fontanella J.C., 1987, in: Proceedings of the workshop on adaptive optics in solar observations. L.E.S.T foundation technical report n°28 September 8-9, Freiburg
Rousset G., Madec P.Y., Rabaud D., 1992, in: Proceedings of E.S.O Symposium on High Resolution Imaging by Interferometry. In: Beckers J.M & Merkle F. (eds.), E.S.O Garching bei Munchen, Allemagne 39, p. 1095-1104,
Soules D.B., Dexter J.J., Waldie A.H., et al., 1989, Proceeding S.P.I.E on propagation engineering. In: Kopeika N.S. and Miller W.B. (eds.), Orlando, FL, p. 224-231
Von-Der-Luhe O., Widener A.L., Rimmele Th., et al., 1989, A&A 224, 351-360